Tribology International 223 (2026) 112192

Contents lists available at ScienceDirect

Tribology International

journal homepage: www.elsevier.com/locate/triboint

Full Length Article

Simulation and validation of the ratcheting effects in B320 and R260MN rails under cyclic wheel–rail contacts

Fang Ren, Zhen Yang, Zili Li *

Delft University of Technology, Stevinweg 1, 2628 CN, Delft, The Netherlands

ARTICLE INFO

Keywords:
Cyclic wheel–rail contact
Finite element analysis
Material ratcheting
Structural ratcheting
Bainitic and pearlitic rail steel

ABSTRACT

The persistent head check (HC) damage in modern railways, a typical form of rolling contact fatigue (RCF), is primarily due to the ratcheting effects in rail. This study employed an efficient and accurate finite element (FE) wheel–rail frictional rolling contact model to simulate the ratcheting effects in rail steels (bainitic B320 and pearlitic R260MN) under 100 cycles of contact loading measured from the HC tests on V-Track test rig. The FE simulation considered both the rail material ratcheting (an intrinsic material property of steel) and structural ratcheting (subjected to altering cyclic contact loading conditions), with the former represented by a calibrated Chaboche constitutive model and the latter captured by the evolving contact patch in the FE simulation. The simulation results were then validated by comparing to the measured running-band width and rail head plastic deformation in the V-Track. A comprehensive analysis of the simulated and measured ratcheting effects confirmed that the bainitic B320 rail exhibited, under the same conditions considered, better anti-RCF performances in terms of slower accumulation of plastic deformation, smaller expansion of the contact patch, and subdued ratcheting rates compared to the R260MN rail. The study also revealed that rail structural ratcheting suppresses the material ratcheting around the longitudinal centreline of the contact patch under the cyclic wheel loading, while at the other locations within the contact patch, the structural ratcheting may intensify the material ratcheting at early cycles, and then suppress it when the contact stresses reach the level of those at the centreline. The ratcheting effects thus showed different patterns to the cases considering material ratcheting alone. Furthermore, the study confirmed that accumulation in residual stresses outside the contact patch can lead to accumulation in plastic strains beyond the rail running band, as the secondary effect of wheel–rail contact.

1. Introduction

Head check (HC) is a common type of rolling contact fatigue (RCF) and significantly challenges modern railways. HC is primarily attributed to rail ratcheting, i.e. the progressive and directional accumulation of plastic deformation induced by repeated wheel-rail contacts [1]. Extensive ratcheting can deplete the ductility of rail steel, and lead to the formation of cracks [2,3], serious HC damage [4] and even disastrous accidents [5]. Therefore, gaining a deeper understanding of ratcheting phenomena in the rails is crucial for mitigating HC damages and ensuring the durability and reliability of railway infrastructure.

To investigate the ratcheting effects in rails, two ratcheting phenomena should be addressed: material and structural ratcheting [6,7]. The material ratcheting is considered as an intrinsic elastoplastic behaviour of the (rail) steels, identifiable by material tests loaded under cyclic homogeneous (proportional) stresses [8–10]. The material ratcheting of rail steels can also be effectively represented by constitutive models that incorporate isotropic and kinematic hardening processes, emulating their elasto-plastic behaviours [8,11–14]. Isotropic hardening/softening describes the expansion/contraction of the yield surface, whereas kinematic hardening replicates the Bauschinger effect, where the yield surface shifts under cyclic loading. Among various constitutive models, the Chaboche model [8,11] has been widely used in cyclic loading simulations [15–19] with its relatively simple formulation and low computational demand. The application of the Chaboche model in the ratcheting simulation of wheel–rail contacts, especially including also the structural ratcheting, has not been extensively studied, encouraging further detailed examination and validation of the model under real-life railway operating conditions.

With respect to structural ratcheting, it concerns the plastic strain accumulated under non-uniformly distributed and varied stress conditions with an increase in load cycles. This is particularly relevant in the context of wheel-rail contact, as the contact patch presents an uneven

* Corresponding author.
E-mail address: Z.Li@tudelft.nl (Z. Li).

https://doi.org/10.1016/j.triboint.2026.112192
Received 28 December 2025; Received in revised form 12 May 2026; Accepted 15 May 2026
Available online 21 May 2026

stress distribution [20,21], and the contact geometry, i.e., the profiles of the wheel and the rail, changes due to plastic deformation [22,23] with contact cycles, leading to alterations in contact stresses in each cycle [19,23]. Therefore, structural ratcheting should be addressed by wheel–rail contact models to capture the rail ratcheting behaviour under real-life cyclic wheel loading conditions. The features of structural ratcheting cannot be fully captured by 2D analytical or finite element (FE) models [15,24,25] that simulate wheel-rail contact as line contact. As to the 3D FE contact models, due to the high computational demand, simplifications have often been made by modelling either one contact body (usually the rail) with prescribed contact stresses [26–29] or small parts of the wheel and rail [30]. They excluded the influence of structural ratcheting from its evolving contact geometry, or simulated only full-slip wheel–rail contact as normal real-life railway operation is with partial-slip wheel–rail contact.

To account for both material and structural ratcheting, this research employed an efficient and accurate wheel-rail cyclic contact model [23] with the rail material represented by a calibrated Chaboche constitutive model [31] to comprehensively study the ratcheting effects in the rails. Two types of rail steels were studied: a newly developed bainitic B320 rail and a conventional pearlitic R260MN rail, with their material ratcheting properties characterised through cyclic material tests [31]. Meanwhile, the ratcheting in these rail steels was investigated experimentally in the V-Track test rig at TU Delft [32]. Ratcheting simulations were performed for up to 100 wheel-rail contact cycles, with the same partial-slip loading conditions measured on the same rail steels in the V-Track. The effects of material and structural ratcheting were then analysed in detail in terms of plastic deformation, the evolution of the contact patch, the contact and equivalent stress states, and ratcheting strains at locations within and beyond the contact patch. The simulated ratcheting effects in the rails were also validated indirectly by comparing them to the measured changes in the width of the running band and rail profile in the V-Track.

2. Methodology

This section first explained the ratcheting simulation procedure, and then described the Chaboche constitutive models calibrated for the two rail steels, focusing on their mechanical and hardening parameters used in the simulations. The determination of the loading conditions for V-Track tests was also detailed in this section. Finally, the approach for validating the simulations was explained.

2.1. FE modelling and simulation procedure

An FE model for the rolling contact simulation was built in LS-DYNA [33] to replicate the wheel–rail setup of the V-Track test rig [34,35], as illustrated in Fig. 1. The V-Track (an overview shown in Fig. 1(a)) features down-scaled wheels running over the rails in a ring track, with the wheels and rails made from the original material [32]. The V-Track can reproduce real-life wheel–rail contact conditions, and has successfully produced various rail damages, including HC, as reported in [32]. Figs. 1(b) and (c) illustrate a comparative view of the wheel-rail setups in the V-Track and FE model in LS-DYNA. The wheel features a cylindrical shape with a radius of 65 mm, whereas the rail head has a designed contact radius of 30 mm. In the FE model, the wheel was simplified as a layer of wheel tread, rigidly connected to the rotating shaft, and the rail was reduced to a partial of the rail head section with a length of 28 mm, as shown in Fig. 1(c). The rolling contact simulations were conducted over a maximum longitudinal distance of 24 mm to prevent potential boundary effects. Contact conditions, plastic deformation and ratcheting effects were evaluated within an interior window between 14–18 mm, where stable and consistent results can be obtained according to the sensitivity studies on the boundary effects and mesh transition [23].

This study employed the same modelling procedure as detailed in [23], which has been optimised and verified for its accuracy and efficiency in cyclic contact simulations. Improvements were made to the FE model represented in [23]. The rigid beams were replaced by the constrained nodal rigid body (CNRB) [33] to connect the flexible wheel tread and the rigid central shaft, as illustrated in Fig. 1(c). This modification further reduced the complexity of the model and improved the computational efficiency. Furthermore, as shown in Fig. 2, the fine mesh region of the rail was extended over the defined contact region (with a mesh size of 0.15 mm) to capture the build-up in residual stresses and strains beyond the contact region (with a mesh size of 0.30 mm) [32]. As in [23], a fine mesh of 0.10 mm was designated along the rail depth to precisely track the shear stress distribution beneath the rail surface.

This study also used the automated simulation procedure described in [23]. The new FE model employed in this study increased the simulation efficiency with one load cycle taking less than 20 min, while 25 min were needed for a one-cycle simulation in [23], using 16 threads of the CPU at its overclocking speed of 3.7 GHz. The procedure can automatically execute the rail ratcheting simulations for a predefined number of wheel load cycles, extract the stress–strain states and irrecoverable nodal displacements, and carry them to the next-cycle simulation, thereby capturing the structural ratcheting that features the changes in contact conditions per cycle. The output from the procedure, including the accumulation of plastic deformation, contact patch evolution, and the ratcheting rates, were extensively investigated to examine the complete ratcheting effects in the two rails of concern in this study.

2.2. Material model

Elastic material was used in the wheel to practically approximate the actual situation on V-Track, as in [23]. The wheel, with a radius of 65 mm and a perimeter of 408.2 mm, undergoes approximately 31 revolutions over the entire 12,560 mm ring track during one loading cycle at a given rail location, as illustrated in Fig. 1(a). Consequently, for a fixed rail position, the wheel is subjected to a substantially higher number of rolling contact cycles. This repeated loading leads to the development and stabilisation of a worn running band and strain hardening of the wheel material much earlier than the rail of the investigated location. Therefore, simulating the change in profile of the wheel that is in contact only with a small section of the rail (24 mm) in this model was unrealistic and unnecessary. Moreover, using the elastic material for the wheel was computationally more efficient for the ratcheting simulation.

To consider the material ratcheting in the rails, the Chaboche nonlinear kinematic hardening (NLKH) model [8] was used, integrated with the VOCE isotropic hardening/softening [8,36], which is available in the LS-DYNA [37]. Table 1 presents the mechanical and hardening parameters used in the Chaboche model for the two rail steels, bainitic B320 and pearlitic R260MN. C_i and γ_i $(i = 1,2,3)$ are the plastic modulus and the plastic strain constants to specify each component of the backstresses [8,38]. The Q and b are the limits of the change in yield stress and the exponent constant that regulates the rate of isotropic softening, respectively. The isotropic softening is indicated by the negative values of Q as shown in Table 1 as the yield stress saturates at σ_y,softened $= \sigma_{y,0} + Q$ with accumulated effective plastic strain.

The hardening parameters of the rail steels were calibrated with uniaxial material tests discussed in [31], which showed that B320 steel has superior mechanical strengths, evident in its limited accumulation of plastic strain during cyclic loading, compared to the pearlitic R260MN steel. According to [31], the calibrated Chaboche model of the B320 rail was able to replicate the elastic shakedown under a stress range equivalent to the traction condition of 0.3 with a normal contact force of $3500N$, higher than the load cases in this study (discussed in Section 2.3). In contrast, R260MN steel produced a much higher

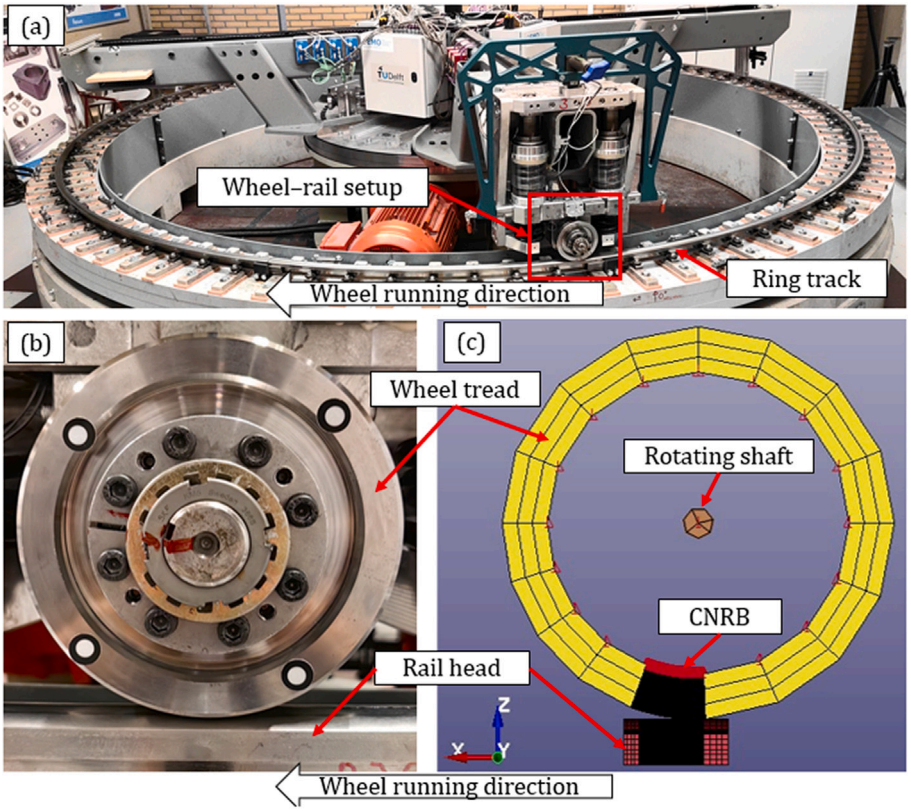

Fig. 1. The V-Track test rig and the corresponding FE model (a) An overview of the V-Track test rig, (b) scaled wheel and rail in the V-Track, and (c) wheel–rail contact model in LS-DYNA.

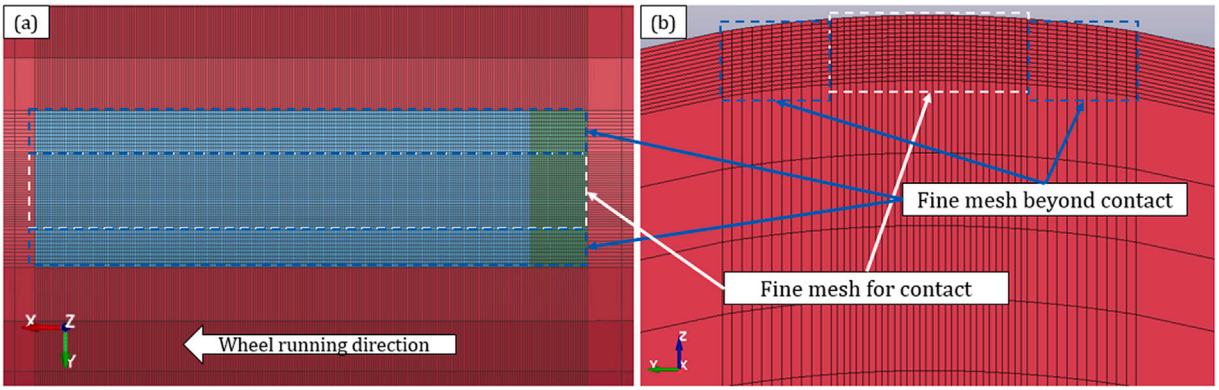

Fig. 2. Fine mesh zones defined in the rail model (a) fine mesh zones defined on the rail surface (top view of the rail model), and (b) fine mesh zones defined in the rail subsurface (cross-section view of the rail model)

material ratcheting strain from the stress range equivalent to the same traction condition, resulting in a very small value of γ_3 (in Table 1) to match the stabilised ratcheting rate of the test, but with an overshoot in the ratcheting strain. We can thus anticipate that the B320 rail will show less ratcheting effects than the R260MN rail in the ratcheting simulations

2.3. Load case

The loading conditions for the simulations were determined at two locations of the V-Track: on the B320 rail section between the sleepers 19 and 22, and on the R260MN rail section between the sleepers 87 and 90. The vertical and longitudinal wheel–rail contact forces measured from the V-Track at different load cycles (cycles 1, 50 and 100) are presented in Fig. 3, together with the coefficient of (CoT), i.e. ratio of the longitudinal force to the vertical force. The lateral force was minimised as controlled below 5% of the longitudinal forces in the HC tests. The contact forces were low-pass filtered at 100 Hz to remove the high-frequency dynamic effects that were less relevant for quasi-static HC initiation [30,39]. As shown in Fig. 3, the variation of the vertical loads for both rails remained low (within 5% of the average load) over the three sleeper span of 376.8 mm. A low-frequency fluctuation remained in the filtered loads, with a characteristic wavelength of approximately 50 mm. Considering that the simulations and validation were conducted over a 24- mm rail segment, this wavelength is significantly larger than the modelled length, supporting the validity of the quasi-static assumption. The potential influence of the longitudinal load variation is further discussed in Section 3.5.2.

Fig. 3 shows that the measured wheel-rail contact forces have good repeatability. The average vertical and longitudinal forces over the

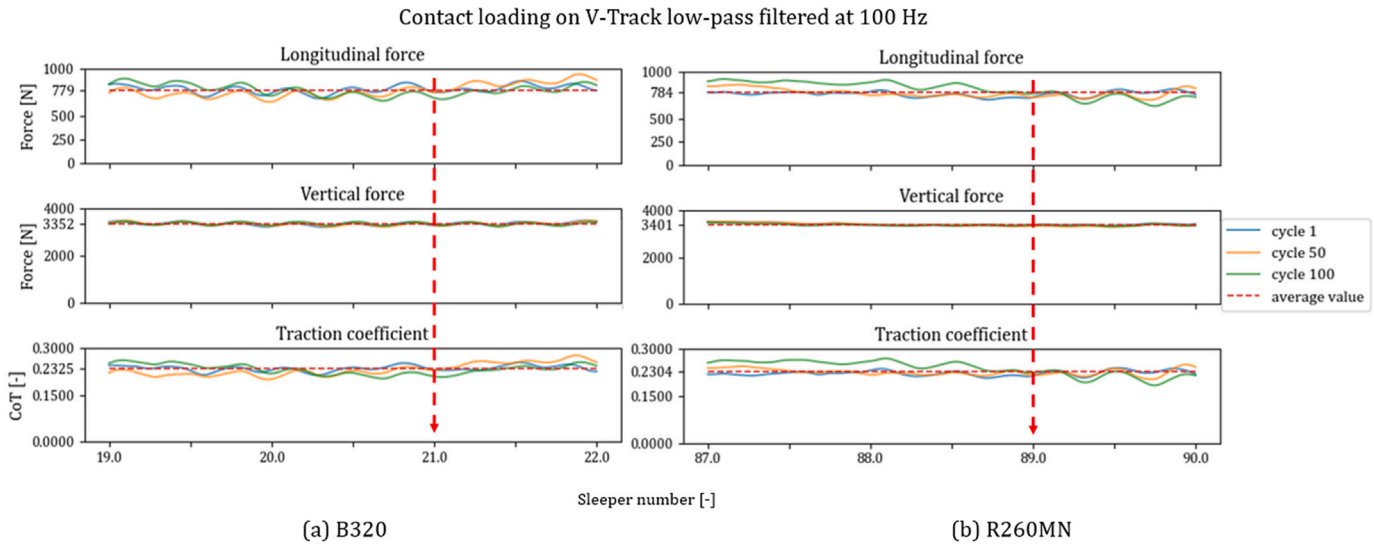

Fig. 3. Longitudinal, vertical forces and the coefficient of traction(CoT) measured from V-Track for (a) B320 and (b) R260MN rails.

Table 1
The mechanical and hardening parameters of R260MN and B320 rail steels [32].

Parameters	R260MN	B320	unit
C_1	461 000	522 000	
C_2	20 000	70 000	MPa
C_3	11 300	15 500	
γ_1	1964	2213	
γ_2	87	240	–
γ_3	28	36	
Q	−167	−220	MPa
b	277	215	–
$\sigma_{y,0}$	348	538	MPa
E	198	196	GPa

three sleeper ranges are $3352N$ and $779N$ for B320, and $3401N$ and $784N$ for R260MN, respectively. The traction coefficients on both rails are around 0.23. These load values were used as loading conditions for the quasi-static FE simulations. Because the loading conditions on the sleeper No. 21 for B320 and No. 89 for R260MN were quite close to these average values (i.e. the simulated loading condition), as indicated by the red dashed arrow in Figs. 3(a) and (b), respectively, the measured ratcheting effects on these two sleepers in the V-Track were used to compare with the simulation results for the validations.

2.4. Validation

This study adopted an indirect validation approach by measuring the evolution of the rail surface running band and cross-sectional profile to assess the ratcheting simulation results. A direct approach based on microscopic analysis of ratcheting strains has been reported in our previous work [32], where the correlation between contact-induced stress conditions (including residual stresses) and ratcheting strain was qualitatively investigated after 60,000 rolling contact cycles. Ratcheting strain – typically indicated by deformation of pearlite lamellae [40] – is difficult to resolve using optical microscopy after only 100 loading cycles, whereas it becomes clearly observable after much larger cycle counts such as 60,000 cycles [32]. Performing such microscopic strain measurements at only 100 cycles would not be practical, considering that our current V-Track HC tests were designed to run for higher numbers of cycles. Therefore, surface and profile measurements provide a more suitable validation approach for this study.

2.4.1. Rail surface change

As a preliminary assessment, the running bands on the rail surfaces were examined with the measured widths compared to the simulated wheel–rail contact patch sizes. As shown in Fig. 4, rail surface images before applying wheel loading and at sleepers No. 21 (B320 Rail) and No. 89 (R260MN) after 100 load cycles were captured, using an ultra-macro lens with a 25- mm focal length and a magnification of 2.5×. These images were post-processed to visually identify the running bands on the rail top surfaces after 100 wheel load cycles. The running bands measured on the B320 and R260MN rails after 100 cycles were 1.99 mm and 2.27 mm in width, respectively.

2.4.2. Rail cross-sectional profile change

The cross-sectional profile changes of the rail heads were captured using a HandyScan 3D black Elite. The scanner setup on the V-Track and a result image during scanning are demonstrated in Figs. 5(a) and (b), respectively. The meshes of the rail surfaces generated by the 3D scan were used to obtain the cross-sectional profiles in the contour graph in the Y-Z plan (normal to the rail longitudinal direction), as shown in Fig. 5(c). The cross-sectional contour curves were then resampled at every 0.05 mm along the Y-axis (in the lateral direction). The resampled cross-sectional profiles were subsequently filtered to remove noise from the scans, as an example shown in Fig. 5(d). The undeformed rail head profiles were reconstructed using the least squared method based on the resampled points from the undeformed surface parts (away from the apparent running band) to determine the original contact radius, R, as indicated in Fig. 5(d). The maximum difference between the deformed and reconstructed 'original' profiles in the Z-axis (in the vertical direction) was identified as the vertical plastic deformation dZ, as shown in Fig. 5(d).

3. Simulation results and validation

This section analysed the simulation results of the ratcheting effects in the two rail steels. The plastic deformations in the rail surface and subsurface, along with the evolution of contact patches, were first analysed and compared between the B320 and R260MN rails. The structural ratcheting represented by the evolving contact and equivalent stresses was then analysed in detail at different locations within and beyond the contact patch. The complete ratcheting effects were further evaluated in terms of the ratcheting strains and rates. Lastly, validation of the simulated ratcheting effects was discussed.

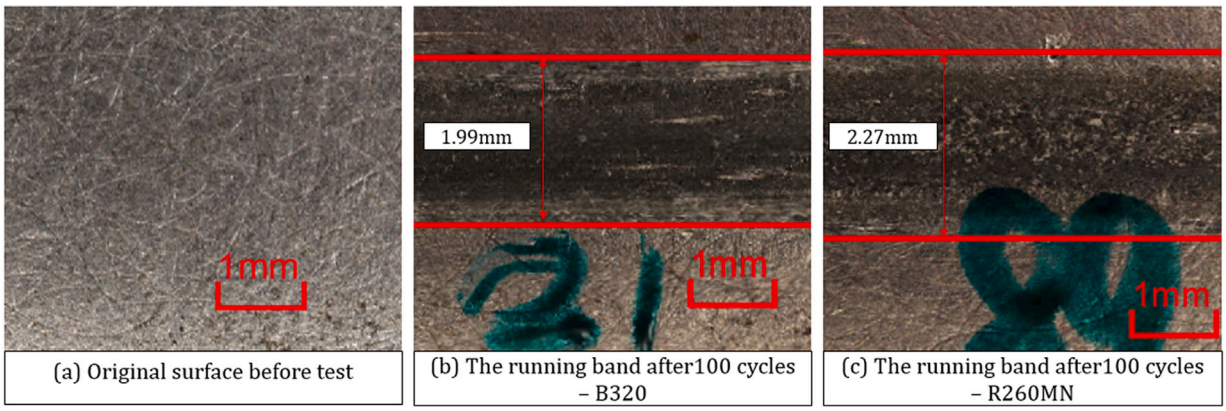

Fig. 4. Rail surface observed from the images: Rail surface observed from the images: (a) rail surface before applying wheel loads, (b) top surface of B320 rail after 100 wheel loads, and (c) top surface of R260MN rail after 100 wheel loads.

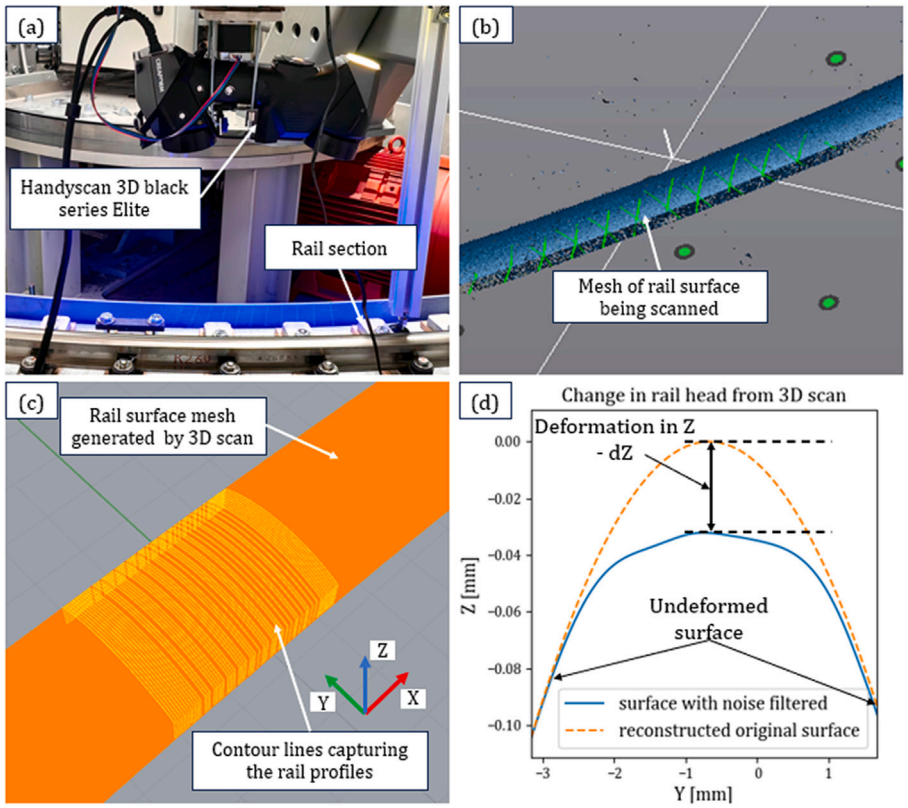

Fig. 5. Rail cross-sectional profile measured with 3D scans: (a) the scanner setup (b) the scanning process (c) the sampling of the profiles from scanning (d) the post-processed rail profile and the deformation in the Z-axis.

3.1. Plastic deformation

Figs. 6 and 7 present the simulated rail head plastic deformation evolution in 100 load cycles for the B320 and R260MN rails, respectively. The same loading conditions were applied, as presented in Section 2.3. We can see that both rails show similar patterns in the development of plastic deformation, which was rapid in earlier cycles (from cycle 1 to cycle 20), then moderated (from cycle 20 to cycle 45, and from 45 to 70), and finally approached stabilisation (after cycle 70). The B320 rail, owing to its superior mechanical strength, produced less plastic deformation than the R260MN rail, as anticipated. The R260MN rail experienced almost twice as much plastic deformation as the B320 in all three axis directions.

Figs. 6(c) and 7(c) also show that for both rails, the contact radii in the lateral direction increased with load cycles due to the accumulation of plastic deformation. An increase in contact radii can then affect contact conditions and solutions, e.g. expanding the contact patches and, at the same time, reducing the contact stresses at the centreline of the contact patch (to be elaborated in the next section). Furthermore, the differences in the Z-axis between the original profile and those during the load cycles indicate to what extent the rail head was plastically deformed in the simulation. The validation of this plastic deformation against the test results is presented in Section 3.5.

3.2. Contact patch evolution

Figs. 8 and 9 compare the wheel–rail elasto-plastic contact solutions of the B320 and R260MN rails to those on the purely elastic rail under the same loading conditions. Both plastically deformed rails have their

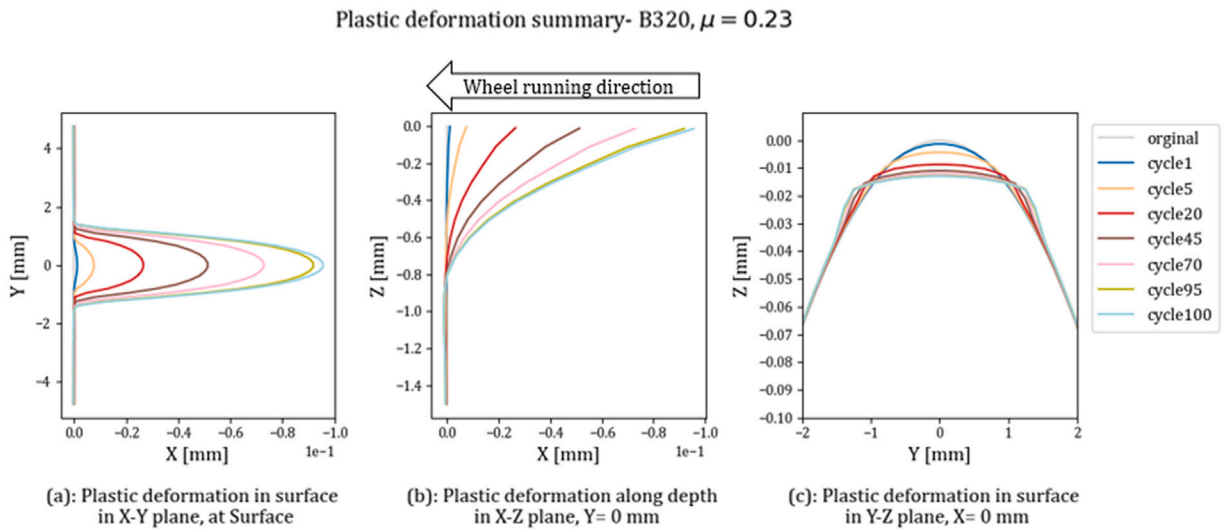

Fig. 6. Simulated accumulation of plastic deformation of B320 rail, (a) plastic deformation in the X-Y plane (b) plastic deformation in the X-Z plane, and (c) plastic deformation in the Y-Z plane.

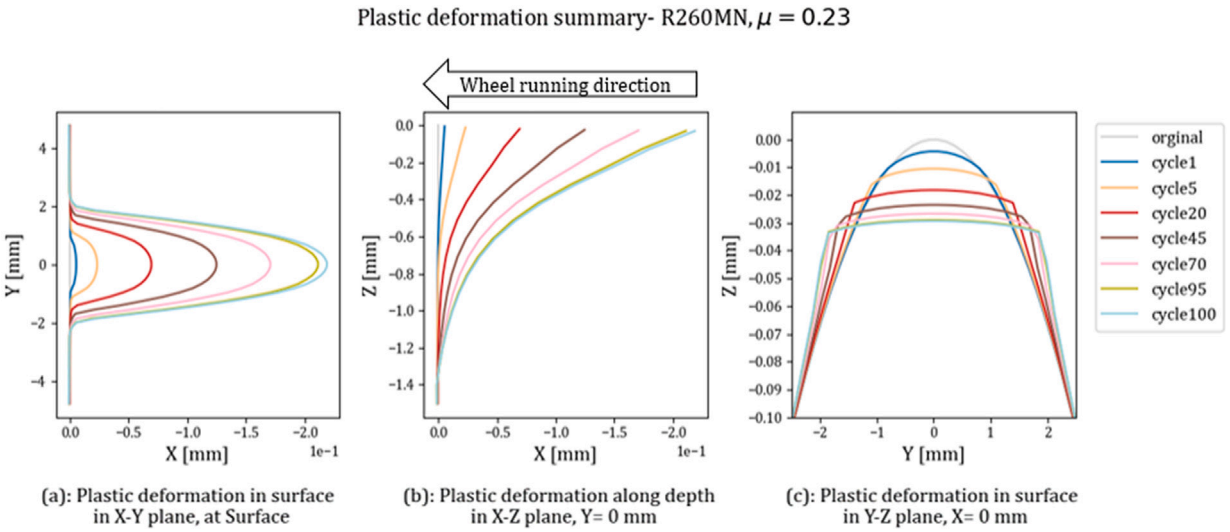

Fig. 7. Simulated accumulation of plastic deformation of R260MN rail, (a) plastic deformation in the X-Y plane (b) plastic deformation in the X-Z plane, and (c) plastic deformation in the Y-Z plane.

peak normal contact pressures leaning towards the leading side of the contact patch, in contrast to the symmetrical contact pressure distribution of the elastic rail. That is because, for the B320 and R260MN rails, the higher shear stresses on the trailing side of the contact patch plastically deformed the rail more than that on the leading side, causing larger expansion of the contact patch on the trailing side and thus with lower contact pressures, thus forming the egg-shaped contact patch with the peak contact pressure shifting forward [41–43]. Therefore, the contact patches of B320 and R260MN rails had egged shapes as compared to the elliptical shape on the elastic rail, as marked by the red dashed ovals in Figs. 8(c) and 9(c).

Furthermore, the B320 rail had contact stresses in the first load cycle close to those of the elastic rail, with their contact patches differing marginally as indicated in Fig. 8(c). This small difference in contact pressures indicated that the plastic deformation in the B320 rail of the first cycle was relatively small due to its higher yield strength. Contrastingly, the R260MN showed much lower contact stresses in the first cycle compared to those of the elastic rail, and the contact patch of R260MN was significantly larger than those of the elastic and B320 rails. The results showed that the use of elastic material can overestimate the actual contact stresses and is thus less suitable for analysing the ratcheting in rail.

The contact patch evolves with increasing load cycles due to plastic deformation as discussed in [22,23]. Figs. 8(c) and 9(c) show the simulated contact patch evolution of B320 and R260MN rails, respectively. With the accumulation of plastic deformation, the contact radii of the rail head increased, as shown in Figs. 6 and 7. This process led to a considerable expansion of the contact patch in the lateral direction and limited shrinkage in the longitudinal direction in 100 wheel load cycles, as shown in Figs. 8(c) and 9(c). The contact patch expansion was more significant in the early cycles, especially within 20 cycles, and approached stabilisation after 70 cycles. For both rails, the contact patches barely changed between the 95th and 100th cycles. This trend aligned well with the development in the accumulation of plastic deformation presented in Figs. 6 and 7.

The change in surface contact stresses on the two rails, as shown in Figs. 8 and 9, followed a similar pattern: the magnitudes of the contact stresses first decreased rapidly, and gradually stabilised after 70 cycles. The stabilised normal and shear stresses were considerably lower than those of the first cycle. Additionally, the contact stresses

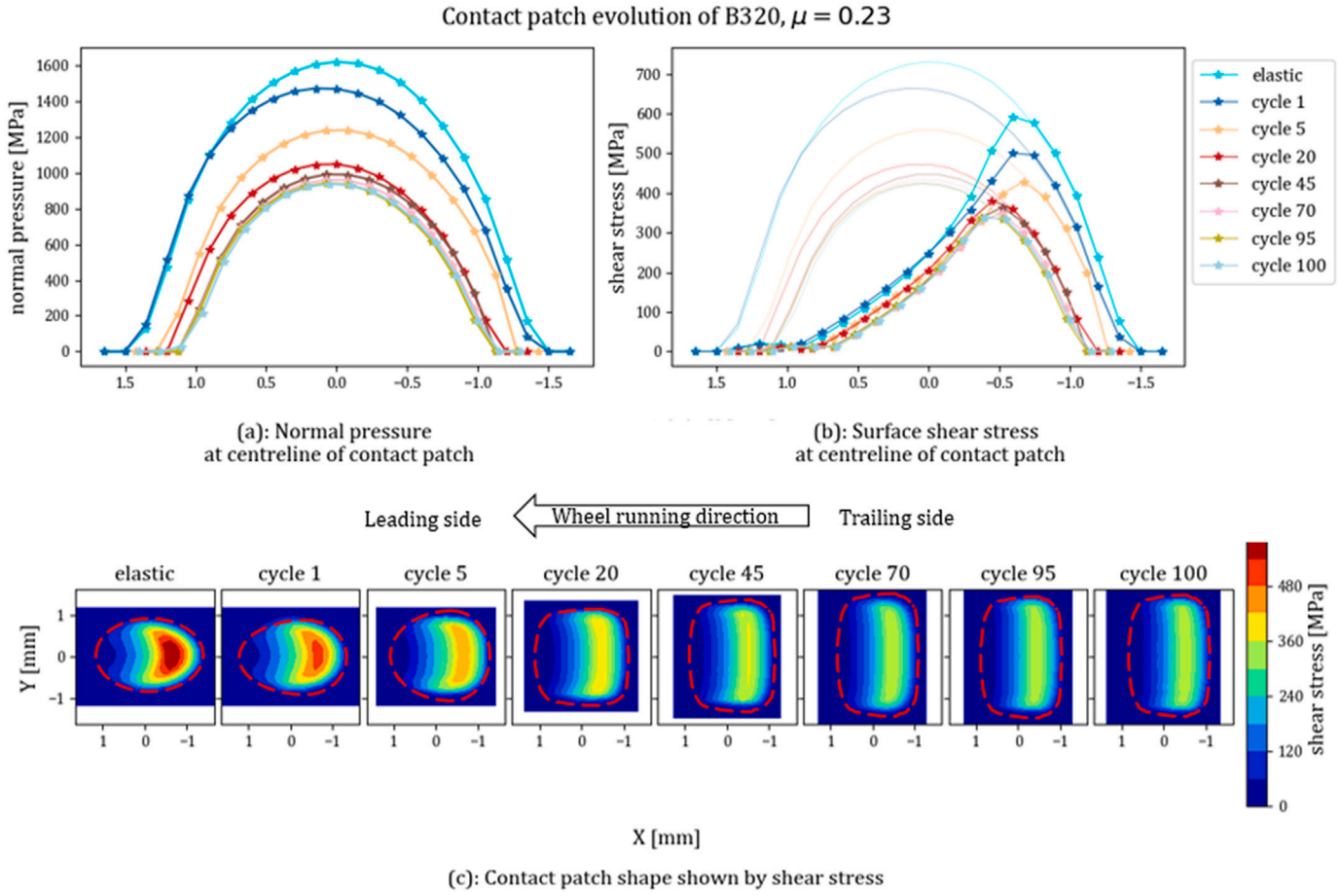

Fig. 8. Contact stresses and contact patch evolution of the B320 rail.

decreased much less significantly in the B320 rail than in the R260MN due to the smaller plastic deformation accumulated over 100 cycles and consequently the smaller expansion in the contact patch.

For the first wheel load cycle, the contact stresses yielded the rail material, initiating material plastic deformation in the rail head. The contact stresses were effectively reduced by the plastic deformation, decelerating material ratcheting at the centreline of the contact patch. Subsequently, the rail head continued to accumulate plastic deformation, leading to further expansion of the contact patch and reduction in contact stresses. Therefore, at the centreline of the contact patch, the material ratcheting gave the structural ratcheting a pattern of decreasing stresses over the cycles; Meanwhile, the structural ratcheting suppressed the material ratcheting by decreasing contact stresses over the load cycles. Eventually, an equilibrium in the change of contact stresses was reached between the material and structural ratcheting so that the decrease in contact stresses and accumulation of plastic deformation stabilised as indicated by the small but steady change in contact stresses between cycles 95 and 100 for both rails shown in Figs. 8(a), (b), 9 (a) and (b).

3.3. Contact induced stresses

To obtain an overview of ratcheting effects in the B320 and R260MN rail heads, we examined both the rail surface contact stresses and the effective stresses of the surface elements at five different lateral (Y) locations: four within and one beyond the contact patch after 100 wheel load cycles, as shown in Figs. 10 and 11, respectively. The black dashed lines in the figures demarcate the stress conditions into three parts: before, during and after contact.

Figs. 10 and 11 show the changes in the surface contact stresses and equivalent stresses of the surface elements at various lateral locations for both rails over the load cycles. The surface shear stresses at the longitudinal centreline of the contact patch, i.e. $Y = 0.0$ mm in Figs. 10 and 11, are the same as those presented in Figs. 8(b) and 9(b) where the comparisons to the elastic solutions are also given. The effective stresses at $Y = 0.0$ mm exceeded the initial yield stresses (538 MPa for B320 and 348 MPa for R260MN, as denoted by the blue horizontal lines) in all load cycles, and their variations followed a similar pattern as the contact stresses: they first decreased rapidly and then gradually stabilised. We can see that the peaks of the equivalent stresses align with those of the contact shear stresses. This confirmed that the contact shear stress contributed the most to material yield [44] within the contact patch [32].

In cycle 1, at the edge of the contact patches, which was $Y = 0.87$ mm for B320 and $Y = 1.02$ mm for R260MN (not yet any surface stresses at further locations), the effective stresses were below the initial yield stresses, indicating that plastic deformation did not occur throughout the contact. At the furthest locations of interest away from the contact patch centreline, no surface contact stresses were present since they were beyond the contact patch, while the contact-induced effective stresses existed with low magnitudes. The after-contact parts of Figs. 10(b) and 11(b) also show that the effective stresses did not diminish after wheel passing, indicating that residual stresses were generated in rails after contact.

In cycle 5, both the contact and effective stresses increased significantly at the contact patch edge locations of cycle 1 ($Y = 0.87$ mm for B320 and $Y = 1.02$ mm for R260MN), indicating that the contact patches expanded and yielded the rails further in the lateral direction. The contact-induced effective stresses beyond the contact patch,

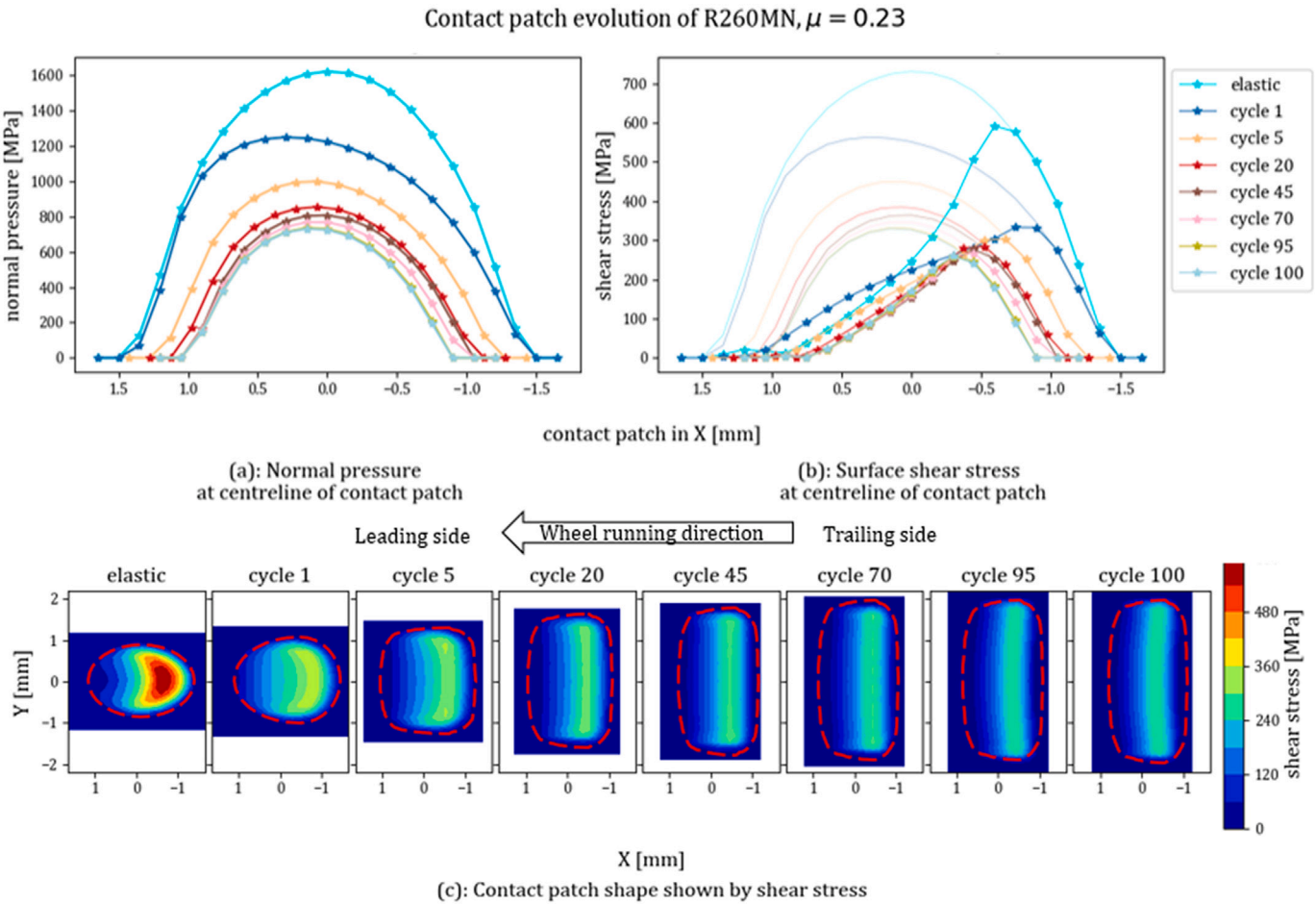

Fig. 9. Contact stresses and contact patch evolution of the 260MN rail.

i.e. over $Y = 0.87$ mm for B320 and $Y = 1.02$ mm for R260MN (with zero surface contact stress), can also be observed. In particular, the effective stress exceeded the initial yield stress on the R260MN rail at $Y = 1.31$ mm, exhibiting the secondary effect of contact discussed in [32]: the compressive wheel-rail contact patch incited tension around it and the accumulation of these residual tensile stresses could also cause the rail to yield.

With a further increase in cycles, we can see that the edge of the contact patch expanded further for both rails, indicated by non-zero surface stresses at further lateral locations. This, meanwhile, caused the surface and effective stresses to decrease at the longitudinal centrelines of the contact patches. Different structural ratcheting patterns can be observed at the other lateral locations than the centreline: the contact stresses first increased until they approached the level at the centreline, then decreased, and eventually stabilised. For instance, by comparing the left two graphs of Fig. 10(a), the surface stresses at $Y = 0.87$ mm for B320 increased with load cycles and reached the same level at the centreline in cycle 20; and then the surface stresses decreased until cycle 70 and stabilised afterwards.

In cycle 100, the half-width of the contact patch expanded beyond 1.31 mm for B320 and 1.45 mm for R260MN, indicated by the non-zero surface stresses. Within the contact patch, the effective stresses within 100 cycles all exceeded the softened yield stress (σ_y,softened $= \sigma_{y,0}+Q$). Beyond the contact patch, we can see that the effective stresses may also exceed the yield stresses at 1.45 mm for B320 and 2.03 mm for R260MN, implying that the plastic deformation could occur from the secondary effects of rolling contact, even though the ratcheting effects within the contact patch appeared to stabilise.

3.4. Ratcheting rate

The ratcheting behaviours of the rails can be quantified in terms of the ratcheting strains and rates, represented by the effective plastic strain accumulated throughout the cycles p^{eff} and the change of the effective plastic strain per cycle dp^{eff}/dN, respectively [26,38,45]. With only the material ratcheting considered, we may expect that the ratcheting rate decreased rapidly and stabilised after a few cycles as exhibited in material ratcheting tests [38,45]. This stabilised ratcheting rate has been used to calculate the critical ratcheting strain and to predict the initiation of RCF cracks [15,26]. The ratcheting simulations of this study revealed some different patterns in the ratcheting strains during wheel–rail rolling contacts when the structural ratcheting was considered.

Fig. 12 shows the ratcheting of the B320 rail at different lateral locations within and beyond the contact patch. At the centreline $Y = 0.0$ mm, the ratcheting rate shown in Fig. 12(b) started at a relatively high value, and then quickly decreased with load cycles, and finally stabilised at 0.0013 after 40 cycles, which is also evident with the linear increase of ratcheting strain shown in Fig. 12(a). This change in ratcheting rate was consistent with the trends in the accumulation of plastic deformation as discussed in Section 3.1 and similar to the material ratcheting behaviour. However, as discussed in Sections 3.2 and 3.3, the change in the ratcheting rate was influenced by not only

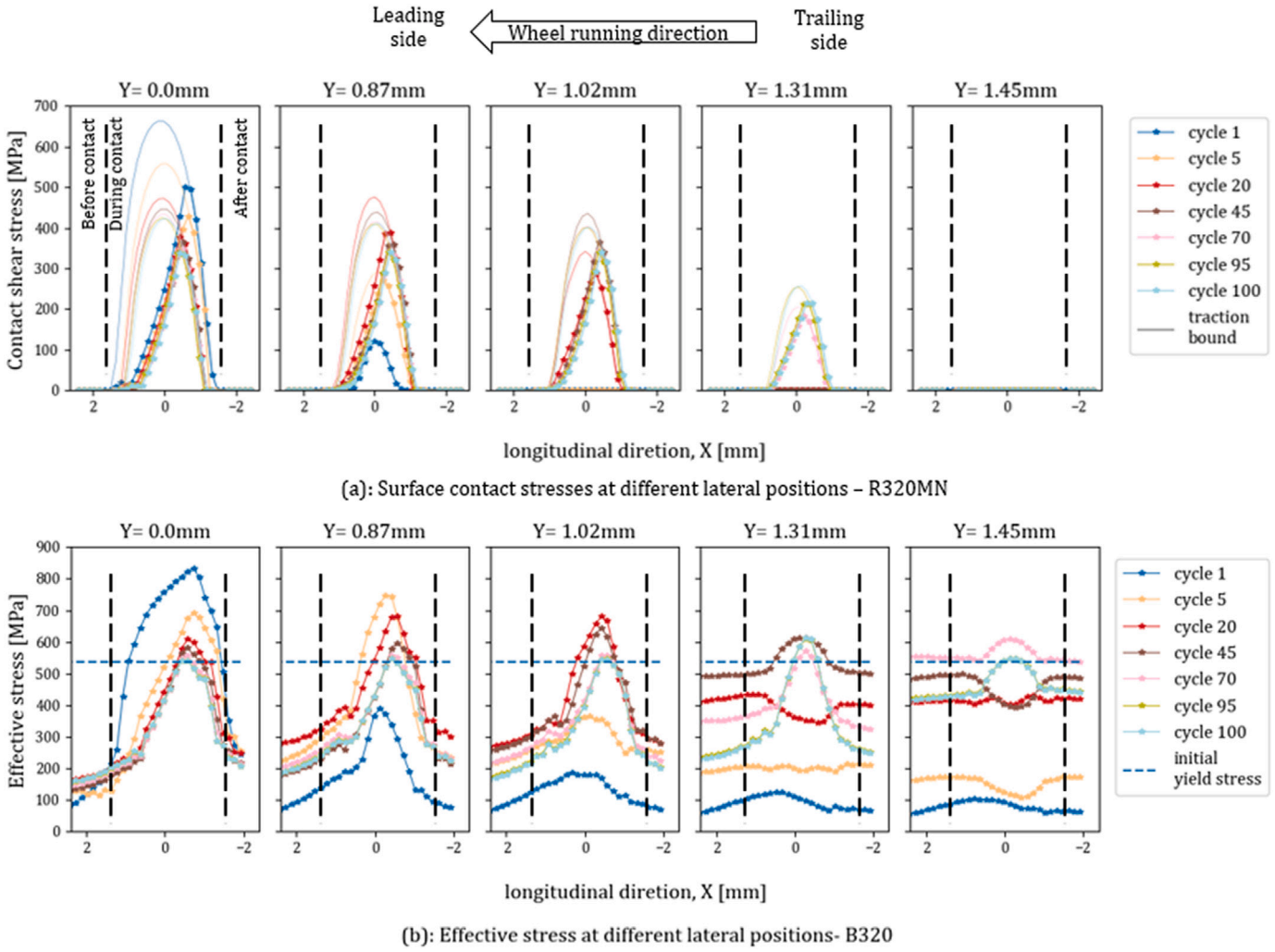

Fig. 10. Stress states in the B320 rail in various load cycles at various lateral locations: (a) contact surface shear stresses and traction bound, and (b) the effective stress of the surface elements.

the material ratcheting of the rail steel but also the structural ratcheting during which the contact stresses decreased with the expansion of the contact patch and thus the material ratcheting was decelerated.

The ratcheting rates in B320 rail at the other lateral locations of the contact patch showed different patterns. For instance, at $Y = 0.87$ mm (likewise at $Y = 1.02$ mm), the ratcheting rate increased with load cycles (in line with the contact stresses increase per Fig. 10) and peaked at cycle 18, and then decreased afterwards, and eventually stabilised at cycle 70 to a similar level of that at the centreline. The change in the ratcheting rate aligned with the trend of the contact surface and effective stresses presented in Section 3.3. At $Y = 1.31$ mm, the ratcheting rate generally increased until it stabilised after 80 cycles. The rail ratcheting behaviours at these locations, i.e. $Y = 0.87$ mm, $Y = 1.02$ mm and $Y = 1.31$ mm, were thus influenced by the structural ratcheting discussed in Section 3.3. Furthermore, at $Y = 1.45$ mm, which was still outside the contact patch at cycle 100, we can observe the onset of plastic deformation in the 53rd cycle. This confirmed that plastic strains can accumulate beyond the contact patch, attributed to the secondary effect of contact discussed in [32].

Similar trends can be observed in Fig. 13 for R260MN rail ratcheting strains and rates. The R260MN rail accumulated higher effective plastic strains, almost twice as much as that of the B320. The stabilised ratcheting rate of R260MN is around 0.0026, while that of B320 is 0.0013 The higher ratcheting rate was expected since the R260MN rail has lower mechanical strengths than the B320 rail with more plastic strain accumulated already at early cycles (c.a. 0.10 for R260MN versus c.a. 0.05 for B320 in 20th cycle), which led to saturation of isotropic softening and softened yield stress at early cycles, further intensifying material ratcheting.

The patterns in the ratcheting rates within the contact patch of both rails underscore the crucial influence of the structural ratcheting at wheel–rail contact. At/around the centreline of the contact patch, the structural ratcheting had a suppressive effect on the rail ratcheting as the ratcheting rate decreased (see in Figs. 12(b) and 13(b)), owing to the expansion of the contact patch and reduction in contact stresses (see in Figs. 10 and 11, $Y = 0.0$ mm). At the locations within the contact patch away from the centreline, the structural ratcheting at early load cycles reinforced the material ratcheting and consequently led to increasing ratcheting rates, as the contact stresses increased with the expansion of the contact patch, causing the rail to yield further. When the contact stresses at these lateral locations reached the level of those at the centreline with the increase of load cycles, the structural ratcheting began to suppress the material ratcheting, which then slowed down the accumulation in plastic deformation and subsequently contact patch evolution. The suppressing effect of structural ratcheting diminished when the equilibrium (as in the change of contact stresses)

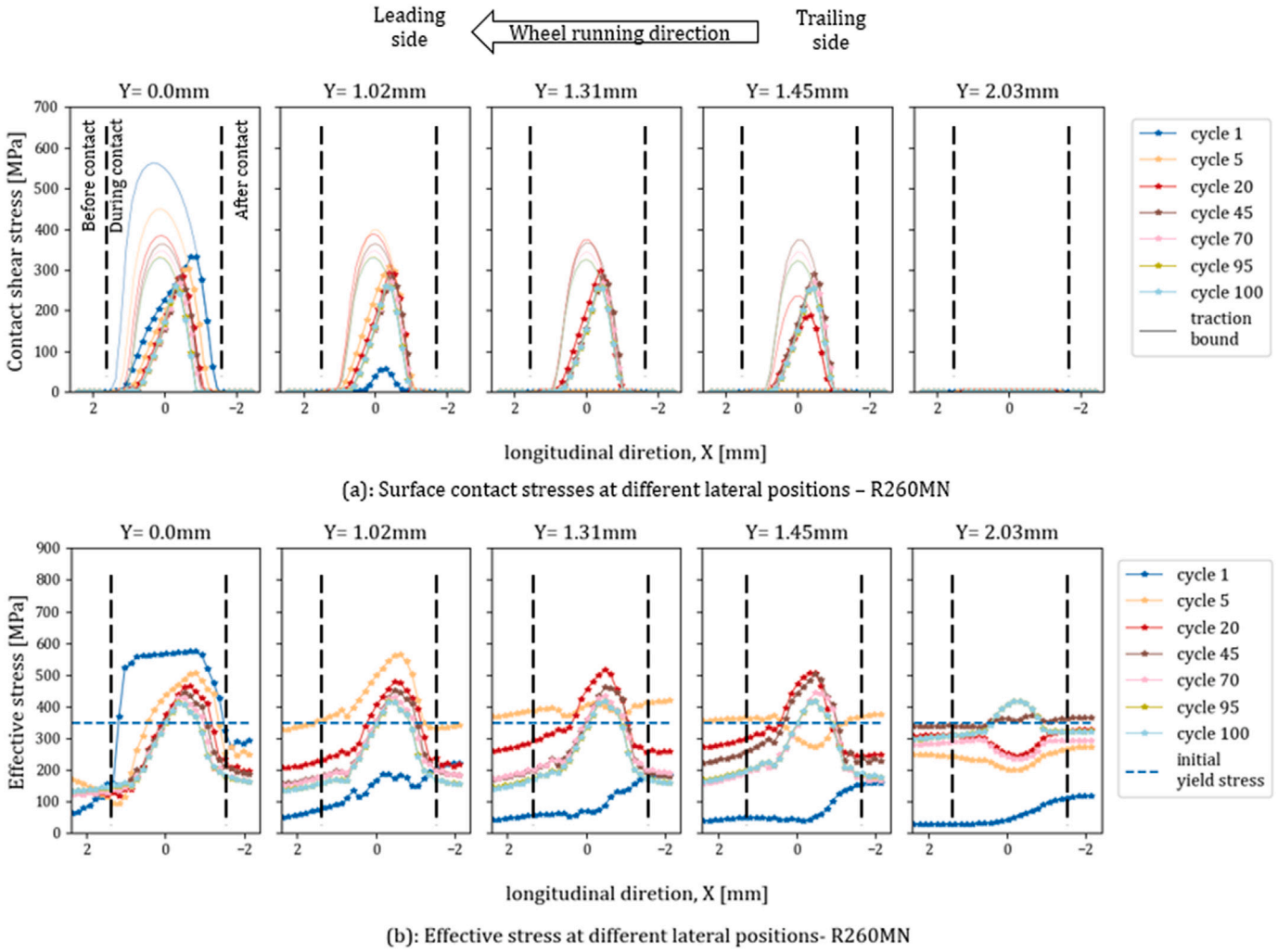

Fig. 11. Stress states in the R260MN rail in various load cycles at various lateral locations: (a) contact surface shear stresses and traction bound, and (b) the effective stress of the surface elements.

was reached between the effects of material ratcheting and structural ratcheting, as indicated by the stabilised ratcheting rates approaching the 100th cycle. Additionally, the present simulation results showed a clear contrast with the fixed-amplitude material ratcheting tests reported in [31], where the prescribed stress paths led to relatively high ratcheting rates in the Chaboche model predictions. In the present contact simulations, however, the ratcheting rate was significantly limited by the structural ratcheting process, particularly around the contact-patch centreline. This comparison highlighted that structural ratcheting can strongly modulate, and in the present case partially suppress, the material ratcheting response under cyclic wheel–rail contact.

The material properties of the two rail steels also play a significant role in their ratcheting behaviour. B320, which possesses a higher yield strength and distinct microstructure [31] compared to R260MN, exhibited lower initial ratcheting strain. As the loading cycles progressed, B320 also showed a lower ratcheting rate, reflecting its higher resistance to material ratcheting [31]. Because material ratcheting in B320 was less pronounced than in R260MN, the suppressing effect of structural ratcheting was correspondingly weaker, as evidenced by the smaller reduction in ratcheting rate observed in Figs. 12 and 13. At $Y = 0.0$ mm, the stabilisation – where material and structural ratcheting effects balance – was reached earlier for B320 (around cycle 45), primarily due to its limited material ratcheting response. In contrast, for R260MN, the ratcheting rate continued to decrease up to approximately 100 cycles. At other locations, structural ratcheting played a more prominent role by intensifying material ratcheting and increasing the ratcheting rate before subsequently suppressing it for both rails. Nevertheless, owing to the inherent material differences, both the ratcheting strain and rate remained lower in B320 than in R260MN.

The two ratcheting processes can be regarded as driven by distinct mechanisms. Material ratcheting refers to the progressive accumulation of plastic strain arising from the intrinsic cyclic plasticity response of the material under a given, repeatable loading path, typically constant-amplitude loading with a mean stress in classical material testing procedures [14,45]. Structural ratcheting, in contrast, refers to progressive plastic strain accumulation driven by cycle-to-cycle changes in the applied stress state, such as increasing stress amplitude or evolving structural loading conditions [6]. In the context of wheel–rail rolling contact, structural ratcheting is not an independent constitutive mechanism, but an emergent contact-geometry-mediated loading-path evolution that modulates the material ratcheting response. It describes the continued plastic strain accumulation resulting from evolving stress conditions associated with contact profile changes. If the material

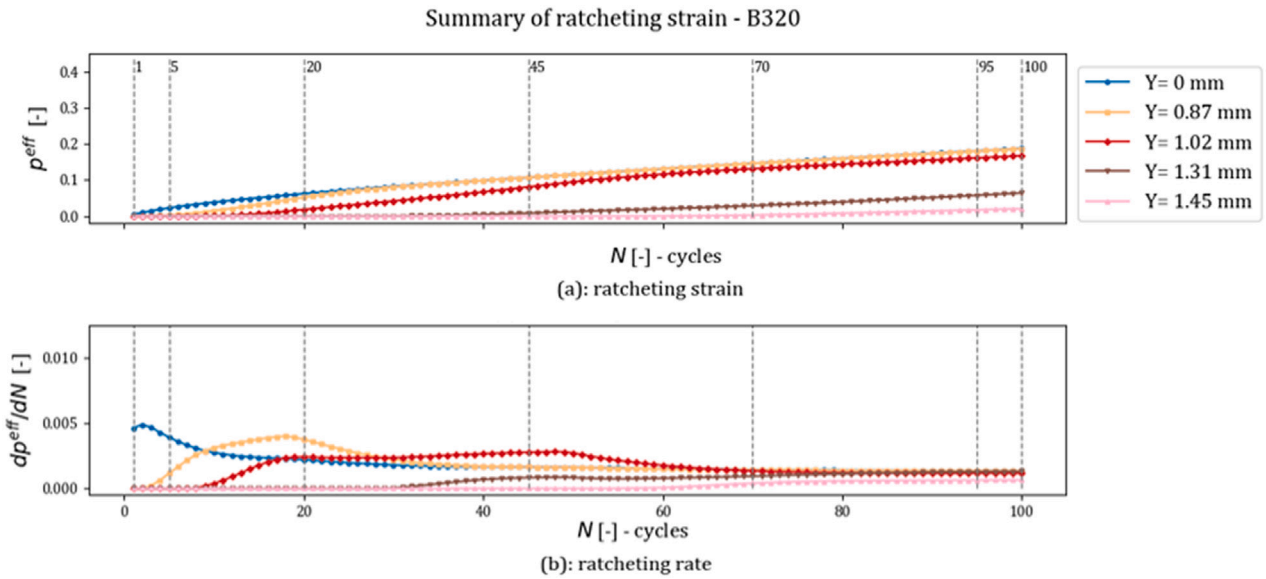

Fig. 12. Ratcheting strain and rate in the B320 rail over the 100 load cycles at five different lateral locations (a) the accumulation of ratcheting strain, and (b) the change of ratcheting rate.

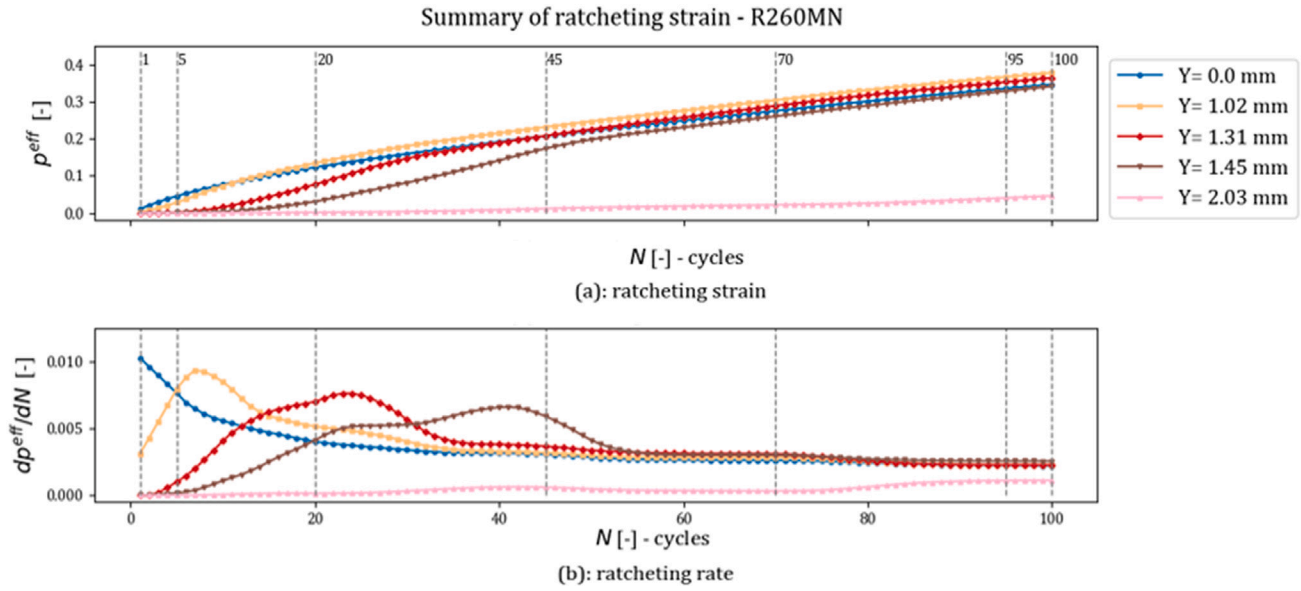

Fig. 13. Ratcheting strain and rate in the R260MN rail over the 100 load cycles at five different lateral locations (a) the accumulation of ratcheting strain, and (b) the change of ratcheting rate.

response became elastic, e.g. shakedown, structural ratcheting would cease. Therefore, the observed stabilisation of the ratcheting rate in rails corresponds to the coupled interaction of material and structural ratcheting, producing persistent – though significantly reduced – rate in plastic strain accumulation and complete shakedown has not been reached over the 100 cycles simulated in this study. This interpretation reflects the temporal aspect of ratcheting behaviour, which has been widely discussed in previous studies [23,26,30] where the contribution of structural ratcheting were often overlooked. However, structural ratcheting at the wheel–rail interface also exhibits an important spatial characteristic. As identified in this study, the evolution of ratcheting may vary across different locations within a contact patch due to local variations in stress conditions driven by the evolving contact patch. This spatial variation provides additional insight into the mechanisms governing ratcheting behaviour in rails.

3.5. Validation

This study took two steps to validate the simulation results. First, the rail running bands observed after the 100th wheel load cycle from the V-Track were compared with the simulated contact patches for both rails. The width of the contact patch was checked against the that of the running band for an initial assessment. Second, the rail top plastic deformation after the 100th cycle in the Z-axis was extracted from 3D scans of the geometry on the V-Track, statistically analysed and compared with the simulated vertical plastic deformation for the B320 rail.

3.5.1. Running band

Fig. 14 shows the simulated contact patches at the 1st and 100th cycles compared with the running bands on the V-Track after 100 cycles for both rails. The white grids indicate the FE mesh size on the rail top

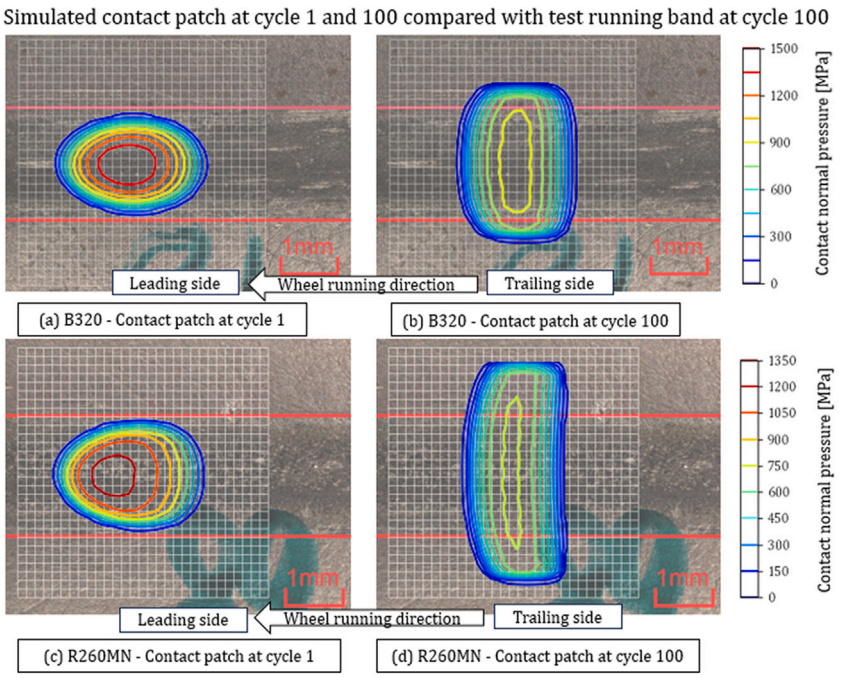

Fig. 14. Simulated contact patch compared with the observed running bands, (a) contact patch of cycle 1 for B320, (b) contact patch of cycle 100 for B320, (c) contact patch of cycle 1 for R260MN, and (d) contact patch of cycle 100 for R260MN.

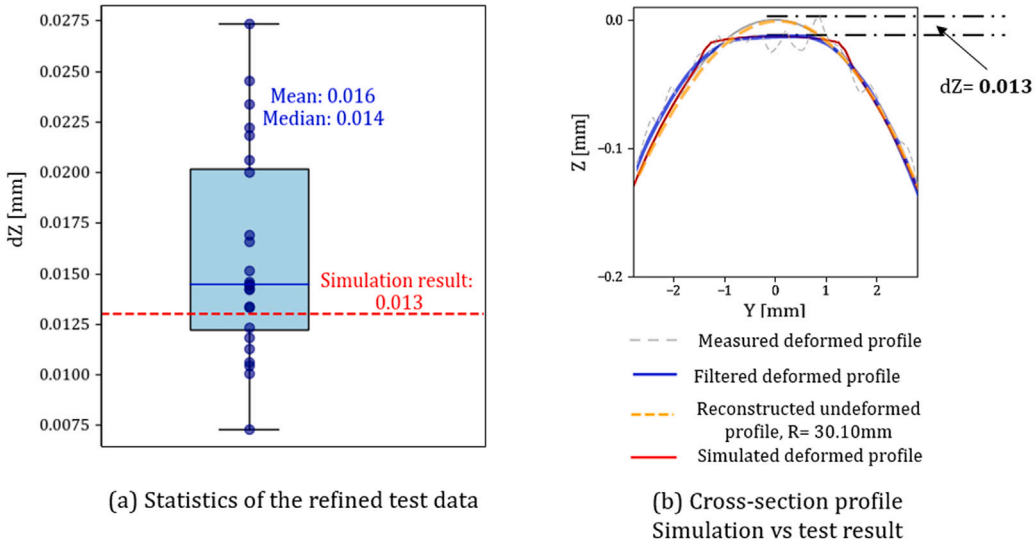

Fig. 15. Step-2 validation results of the vertical plastic deformation: (a) statistics of the refined test data vs the simulated result, and (b) a deformed B320 rail cross-sectional profile vs simulated rail profile.

surface, which is $0.15mm \times 0.15$ mm. The contact patches on both rails of the first cycle can fit well within the observed running bands in Figs. 14(a) and (c), demonstrating the reliability of using the FE method and V-Track test rig to study wheel–rail contact.

Figs. 14(b) and (d) compare the simulated contact patches with the observed running band after the 100th cycle. The simulated contact patch on the B320 rail slightly exceeded (with three elements on each side) the running band, whereas that on the R260MN rail was much wider (approximately 6 elements on each side) than the observed running band. The B320 rail had relatively limited expansion in the contact patch, as also indicated in Fig. 8(c), owing to its high yield stress and subdued material ratcheting behaviour [31]. The overestimation of the contact patch expansion for R260MN could be attributed to the excessive plastic strains induced by the material ratcheting represented by the Chaboche model. As discussed in Section 2.2, the hardening properties of the Chaboche model for R260MN could result in an overshoot in replicating the ratcheting strains, causing plastic deformation and consequently the size of the contact patch to be overestimated, especially within 20 cycles (as shown in Fig. 9), in the rail ratcheting simulation. Therefore, the simulation results of the R260MN rail plastic deformation were not further compared with the test in the second step of validation.

3.5.2. Plastic deformation in Z-axis

30 rail cross-sectional profiles were selected from the scanned rail surface in a 5-cm range over the sleeper NO. 21 of the B320 rail based on random selection and then analysed. The reconstructed contact radii of original rail profiles (R) and the vertical plastic deformation(dZ) after 100 load cycles were post-processed from the selected profiles. The

reconstructed radii of the original rail profiles ranged from 29.40 mm to 30.40 mm, with a median of 29.76 mm and a mean of 29.80 mm while the (design) radius used in the FE rail model was 30 mm. The vertical plastic deformation, determined by comparing the deformed and the reconstructed original rail profiles, as demonstrated in Fig. 5(d), varied from 0.005 mm to 0.030 mm with the average at 0.017 mm and median at 0.015 mm.

Since the contact radii R of the 30 selected rail profiles were distributed over a relatively large range of 1 mm with a median value (29.76) smaller than design radius, a further selection was made considering the R in a 3% range over design radius of 30 mm for a better comparison with the simulated results. The corresponding vertical plastic deformation dZ ranged from 0.0075 mm to 0.0275 mm with a median of 0.014 mm and a mean of 0.016 mm, as the statistics shown in Fig. 15(a). The difference in the plastic deformation among the cross-sections can be caused by the fluctuation of wheel–rail contact forces shown in Fig. 3, which possibly resulted in the variation in the plastic deformation and wear along the rail in the V-Track. As indicated by a red horizontal line in Fig. 15(a), the simulation result of dZ is 0.013 mm, which was determined based on the simulated surface plastic deformation in Fig. 6(c). Fig. 15(b) compares the simulated deformed rail profile to one measured profiles with a R of 30.10 mm, both attaining a dZ of 0.013 mm. More measured deformed profiles can been seen in Appendix. The good agreement between the simulated and measured rail plastic deformation under 100 wheel load cycles confirmed that the effectiveness of the proposed modelling framework to investigate rail ratcheting effects and to predict the initiation of HC cracks.

4. Conclusions and further research

This study addressed both the material and structural ratcheting to elucidate the ratcheting effects observed in rails subject to cyclic wheel–rail rolling contacts. Employing the Chaboche material models to represent two rail steels, i.e. B320 and R260MN, in an efficient and accurate FE frictional rolling contact model, both the ratcheting processes were incorporated in the cyclic wheel–rail contact simulations. The wheel–rail frictional rolling contacts were simulated up to 100 cycles using the same loading conditions as measured from a V-Track test that was designed to generate real-life rail ratcheting and head checks. Furthermore, the running-band width and rail head plastic deformation from the V-Track were measured to validate the simulated wheel–rail contact solutions and rail ratcheting behaviours. The good agreement between the simulations and measurements supports the effectiveness of the proposed modelling framework to investigate rail ratcheting effects for predicting the initiation of HC cracks. The primary findings are summarised as follows.

- The wheel-rail contact stresses are reduced under cyclic wheel loading when the plasticity in the rail steels occurs, since the plastic deformation increases the size of the contact patch, with other things equal. This cannot be considered by linear elastic material models.
- The distribution of contact shear stress for a 3D wheel–rail contact leads to uneven deformation at the contact interface with higher plastic deformation at the trailing end of the contact patch. This pattern in plastic deformation results in an egged shape of the contact patch with the maximum normal contact pressure shifted to the leading end, compared to the symmetrical and elliptical contact patch solved using elastic material.
- The ratcheting simulation over the 100 load cycles concluded that the B320 rail outperformed the R260MN rail steel in terms of RCF resistance as it exhibited lower level of plastic deformation accumulation, smaller contact patch expansion, and subdued ratcheting effects.
- The simulation results highlighted the interplay between the structural and material ratcheting vary with the location within the contact patch: at the longitudinal centreline, the structural ratcheting suppresses the material ratcheting with decreasing contact stresses over the load cycles; and at the other lateral locations away from the centreline in the contact patch, the structural ratcheting may intensify the material ratcheting at early cycles and subsequently suppress it once the contact stresses reach the level of those at the centreline.
- The ratcheting effect in the rail stabilises when the equilibrium in the change of contact stresses influence by the material and structural ratcheting is reached, showing different patterns as compared to the cases simulated only considering the material ratcheting.
- The ratcheting simulations also revealed that the residual stresses can be accumulated outside the contact patch, thereby demonstrating the secondary effect from the wheel–rail contact, i.e. rail steel yield outside the running band.

In this study, the Chaboche constitutive model was used to replicate the material ratcheting, potentially leading to an overestimation of plastic strains and material ratcheting, especially for the soft rail steels with large ratcheting rate, as discussed in [38] and also observed in the simulation results of this study: the simulated contact patch of the R260MN rail was considerably wider than the actual running band observed on the V-Track. Therefore, it is essential for future studies to incorporate more advanced constitutive models, such as Ohno-Wang II (OWII) or Abdel-Karim-Ohno models [12,14], in the FE simulations for the ratcheting effects of R260MN rail [29,46]. Furthermore, to conclusively validate the accuracy of the proposed modelling framework in predicting ratcheting effects, the next phase of research should implement a direct validation method, e.g. deriving the ratcheting strains of the tested rail samples cut from the V-Track based on microscopic examinations [32].

CRediT authorship contribution statement

Fang Ren: Writing – original draft. **Zhen Yang:** Writing – review & editing. **Zili Li:** Writing – review & editing.

Declaration of competing interest

The authors declare that they have no known competing financial interests or personal relationships that could have appeared to influence the work reported in this paper.

Acknowledgement

This research is part of the Maximise Rail Life (MaxLife) project (Code: 15796), conducted at Delft University of Technology, and funded by Dutch rail infrastructure manager, ProRail and the Dutch Research Council (NWO).

Appendix

A selection of 16 post-processed rail profiles used for validation is presented in Fig. 16

Data availability

Data will be made available on request.

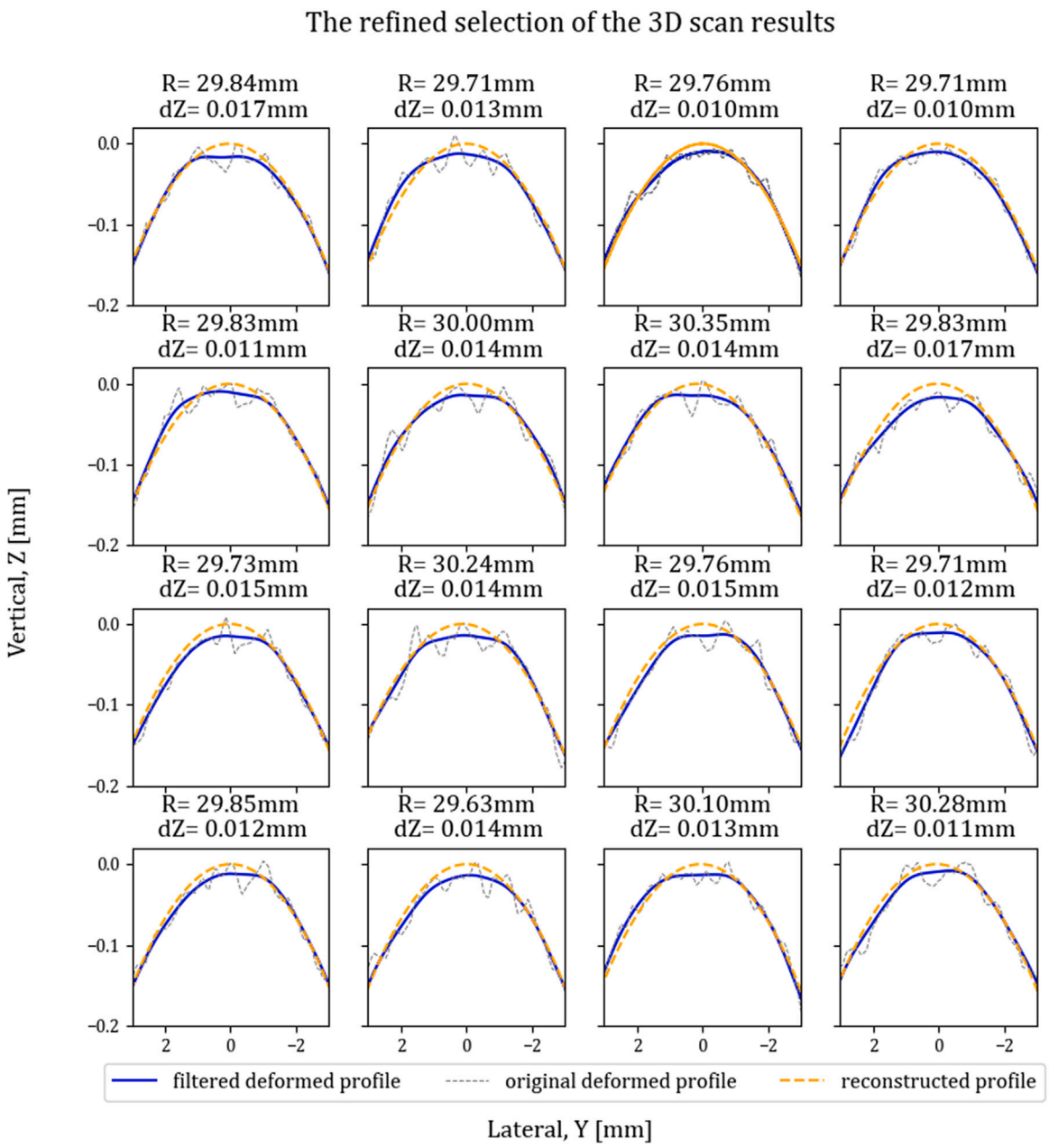

Fig. 16. 16 cross-section profiles post-processed from the 3D-scanned rail top surface of B320.

References

[1] Bower A, Johnson K. The influence of strain hardening on cumulative plastic deformation in rolling and sliding line contact. J Mech Phys Solids 1989;37(4):471–93. http://dx.doi.org/10.1016/0022-5096(89)90025-2.

[2] Eadie DT, Elvidge D, Oldknow K, Stock R, Pointner P, Kalousek J, Klauser P. The effects of top of rail friction modifier on wear and rolling contact fatigue: Full-scale rail-wheel test rig evaluation, analysis and modelling. Wear 2008;265(9–10):1222–30. http://dx.doi.org/10.1016/j.wear.2008.02.029.

[3] Donzella G, Faccoli M, Mazzù A, Petrogalli C, Roberti R. Progressive damage assessment in the near-surface layer of railway wheel-rail couple under cyclic contact. Wear 2011;271(1–2):408–16. http://dx.doi.org/10.1016/j.wear.2010.10.042.

[4] Fletcher D, Franklin F, Kapoor A. Rail surface fatigue and wear. In: Lewis R, Olofsson U, editors. Wheel–rail interface handbook. Elsevier; 2009, p. 280–310. http://dx.doi.org/10.1533/9781845696788.1.280.

[5] Grassie SL. Rolling contact fatigue on the British railway system: treatment. Wear 2005;258(7–8):1310–8. http://dx.doi.org/10.1016/j.wear.2004.03.065.

[6] Hübel H. Basic conditions for material and structural ratcheting. Nucl Eng Des 1996;162(1):55–65. http://dx.doi.org/10.1016/0029-5493(95)01136-6.

[7] Paul SK. A critical review of experimental aspects in ratcheting fatigue: microstructure to specimen to component. J Mater Res Technol 2019;8(5):4894–914. http://dx.doi.org/10.1016/j.jmrt.2019.06.014, URL https://www.sciencedirect.com/science/article/pii/S2238785419300900.

[8] Chaboche J. Time-independent constitutive theories for cyclic plasticity. Int J Plast 1986;2(2):149–88. http://dx.doi.org/10.1016/0749-6419(86)90010-0.

[9] Bower A. Cyclic hardening properties of hard-drawn copper and rail steel. J Mech Phys Solids 1989;37(4):455–70. http://dx.doi.org/10.1016/0022-5096(89)90024-0.

[10] Hassan T, Kyriakides S. Ratcheting in cyclic plasticity, part I: Uniaxial behavior. Int J Plast 1992;8(1):91–116. http://dx.doi.org/10.1016/0749-6419(92)90040-j.

[11] Frederick CO, Armstrong PJ. A mathematical representation of the multiaxial Bauschinger effect. Mater High Temp 2007;24(1):1–26. http://dx.doi.org/10.3184/096034007x207589.

[12] Ohno N, Wang J. On modelling of kinematic hardening for ratcheting behaviour. Nucl Eng Des 1995;153(2–3):205–12. http://dx.doi.org/10.1016/0029-5493(95)90012-8.

[13] Jiang Y, Sehitoglu H. Modeling of cyclic ratchetting plasticity, part I: Development of constitutive relations. J Appl Mech 1996;63(3):720–5. http://dx.doi.org/10.1115/1.2823355.

[14] Abdel-Karim M. Modified kinematic hardening rules for simulations of ratchetting. Int J Plast 2009;25(8):1560–87. http://dx.doi.org/10.1016/j.ijplas.2008.10.004.
[15] Ringsberg J. Prediction of fatigue crack initiation for rolling contact fatigue. Int J Fatigue 2000;22(3):205–15. http://dx.doi.org/10.1016/S0142-1123(99)00125-5.
[16] Pletz M, Daves W, Yao W, Kubin W, Scheriau S. Multi-scale finite element modeling to describe rolling contact fatigue in a wheel–rail test rig. Tribol Int 2014;80:147–55. http://dx.doi.org/10.1016/j.triboint.2014.07.005.
[17] Mohammadpour A, Chakherlou T. Numerical and experimental study of an interference fitted joint using a large deformation chaboche type combined isotropic–kinematic hardening law and mortar contact method. Int J Mech Sci 2016;106:297–318. http://dx.doi.org/10.1016/j.ijmecsci.2015.10.012.
[18] Hwang J-H, Kim Y-J, Kim J-W, Kim S-E. Initial cyclic hardening behavior of cracked structures under large-amplitude cyclic loading. Eng Fract Mech 2021;254:107911. http://dx.doi.org/10.1016/j.engfracmech.2021.107911.
[19] Wu Y, Zhao J, Miao H, Zhang X, Wen Z, Xu J, Wang P, Kan Q. 3D rolling contact finite element analysis of high-speed railway turnout considering ratchetting effect. Eng Fail Anal 2024;160:108171. http://dx.doi.org/10.1016/j.engfailanal.2024.108171.
[20] Zhao X, Li Z. The solution of frictional wheel–rail rolling contact with a 3D transient finite element model: Validation and error analysis. Wear 2011;271(1–2):444–52. http://dx.doi.org/10.1016/j.wear.2010.10.007.
[21] Wei Z, Z. L, Qian Z, Chen R, Dollevoet R. 3D FE modelling and validation of frictional contact with partial slip in compression-rolling evolution. Int J Rail Transp 2015;4(1):20–36. http://dx.doi.org/10.1080/23248378.2015.1094753.
[22] Kapoor A, Johnson K. Effect of changes in contact geometry on shakedown of surfaces in rolling/sliding contact. Int J Mech Sci 1992;34(3):223–39. http://dx.doi.org/10.1016/0020-7403(92)90073-p.
[23] Ren F, Yang Z, Li Z. An efficient 3D finite element procedure for simulating wheel–rail cyclic contact and ratcheting. Tribol Int 2024;109878. http://dx.doi.org/10.1016/j.triboint.2024.109878.
[24] Kapoor A, Beynon JH, Fletcher DI, Loo-Morrey M. Computer simulation of strain accumulation and hardening for pearlitic rail steel undergoing repeated contact. J Strain Anal Eng Des 2004;39(4):383–96. http://dx.doi.org/10.1243/0309324041223935.
[25] Daves W, Kubin W, Scheriau S, Pletz M. A finite element model to simulate the physical mechanisms of wear and crack initiation in wheel/rail contact. Wear 2016;366–367:78–83. http://dx.doi.org/10.1016/j.wear.2016.05.027.
[26] Pun CL, Kan Q, Mutton PJ, Kang G, Yan W. An efficient computational approach to evaluate the ratcheting performance of rail steels under cyclic rolling contact in service. Int J Mech Sci 2015;101–102:214–26. http://dx.doi.org/10.1016/j.ijmecsci.2015.08.008.
[27] Zhou Y, Wang S, Wang T, Xu Y, Li Z. Field and laboratory investigation of the relationship between rail head check and wear in a heavy-haul railway. Wear 2014;315(1–2):68–77. http://dx.doi.org/10.1016/j.wear.2014.04.004, URL http://dx.doi.org/10.1016/j.wear.2014.04.004.
[28] Su H, Pun CL, Mutton P, Kan Q, Yan W. Numerical study on the ratcheting performance of heavy haul rails in curved tracks. Wear 2019;436–437:203026. http://dx.doi.org/10.1016/j.wear.2019.203026.
[29] Li Y, Wu Y, Mutton P, Qiu C, Yan W. A ratcheting mechanism-based numerical model to predict damage initiation in twin-disc tests of premium rail steels. Eng Fail Anal 2023;146:107066. http://dx.doi.org/10.1016/j.engfailanal.2023.107066.
[30] Pletz M, Meyer KA, Künstner D, Scheriau S, Daves W. Cyclic plastic deformation of rails in rolling/sliding contact –quasistatic FE calculations using different plasticity models. Wear 2019;436–437:202992. http://dx.doi.org/10.1016/j.wear.2019.202992.
[31] Ren F, Yang Z, Li Z. Experimental investigation and constitutive modelling of the mechanical and ratcheting properties in rail steels. Intell Transp Infrastruct 2025;4. http://dx.doi.org/10.1093/iti/liaf011.
[32] Ren F, Yang Z, Li Z. Experimental and numerical investigation into rolling contact fatigue crack initiation on the V-Track test rig. Eng Fail Anal 2025;170:109206. http://dx.doi.org/10.1016/j.engfailanal.2024.109206.
[33] LS-dyna keyword user's manual volume II material models. Livermore Software Technology; 2020.
[34] Zhang P, Moraal J, Li Z. Design, calibration and validation of a wheel-rail contact force measurement system in V-Track. Measurement 2021;175:109105. http://dx.doi.org/10.1016/j.measurement.2021.109105.
[35] Naeimi M, Li Z, Petrov RH, Sietsma J, Dollevoet R. Development of a new downscale setup for wheel-rail contact experiments under impact loading conditions. Exp Tech 2017;42(1):1–17. http://dx.doi.org/10.1007/s40799-017-0216-z.
[36] Voce E. A practical strain hardening function. Metallurgia 1955;51:219–26.
[37] LS-Dyna keyword user's manual volume I. Livermore Software Technology; 2020.
[38] Bari S, Hassan T. Anatomy of coupled constitutive models for ratcheting simulation. Int J Plast 2000;16(3–4):381–409. http://dx.doi.org/10.1016/s0749-6419(99)00059-5.
[39] Popov VL. Contact mechanics and friction. Springer Berlin Heidelberg; 2010, p. 301–22. http://dx.doi.org/10.1007/978-3-642-10803-7.
[40] Tyfour WR, Beynon JH, Kapoor A. Deterioration of rolling contact fatigue life of pearlitic rail steel due to dry-wet rolling-sliding line contact. Wear 1996;197(1–2):255–65. http://dx.doi.org/10.1016/0043-1648(96)06978-5.
[41] Zhao X, Li Z. A three-dimensional finite element solution of frictional wheel–rail rolling contact in elasto-plasticity. Proc Inst Mech Eng Part J: J Eng Tribol 2014;229(1):86–100. http://dx.doi.org/10.1177/1350650114543717.
[42] Wei Z, Shen C, Li Z, Dollevoet R. Wheel–rail impact at crossings: Relating dynamic frictional contact to degradation. J Comput Nonlinear Dyn 2017;12(4). http://dx.doi.org/10.1115/1.4035823.
[43] Yang Z, Deng X, Li Z. Numerical modeling of dynamic frictional rolling contact with an explicit finite element method. Tribol Int 2019;129:214–31. http://dx.doi.org/10.1016/j.triboint.2018.08.028.
[44] Mises Rv. Mechanik der festen körper im plastisch- deformablen zustand. Nachr Von der Ges Wiss Gött Math-Phys Kl 1913;1913:582–92, URL http://eudml.org/doc/58894.
[45] Pun CL, Kan Q, Mutton PJ, Kang G, Yan W. Ratcheting behaviour of high strength rail steels under bi-axial compression–torsion loadings: Experiment and simulation. Int J Fatigue 2014;66:138–54. http://dx.doi.org/10.1016/j.ijfatigue.2014.03.021.
[46] Zhou Z, Li W, Wen Z, Zhou S, Tao G. Three-dimensional elastic–plastic stress analysis of wheel–rail cyclic rolling contact using finite element method. Wear 2024;542–543:205277. http://dx.doi.org/10.1016/j.wear.2024.205277.